

^{31}P NMR studies of the $\frac{1}{3}$ -depleted two-dimensional anisotropic kagome lattice system $\text{BaCu}_2(\text{PO}_4)_2(\text{H}_2\text{O})$

V. K. Singh ^{1,*,\dagger} J. Link ^{2,\dagger} K. Kargeti,³ S. K. Panda,³ I. Heinmaa ² C. Dhanasekhar ⁴ Monika Jawale ⁴ Kwang-Tak Kim,⁵ Kee Hoon Kim,^{5,6} T. Chakrabarty ⁷ A. V. Mahajan ⁴ R. Stern ² and B. Koteswararao ^{1,\ddagger}

¹*Department of Physics, Indian Institute of Technology Tirupati, Tirupati 517506, India*

²*National Institute of Chemical Physics and Biophysics, Tallinn 12618, Estonia*

³*Department of Physics, Bennett University, Greater Noida, Uttar Pradesh 201310, India*

⁴*Department of Physics, Indian Institute of Technology Bombay, Powai, Mumbai 400076, India*

⁵*Department of Physics and Astronomy, Seoul National University, Seoul 151-747, Republic of Korea*

⁶*Institute of Applied Physics, Department of Physics and Astronomy, Seoul National University, Seoul 151-747, Republic of Korea*

⁷*Division of Sciences, Krea University, Sri City, Andhra Pradesh 517646, India*



(Received 1 February 2024; revised 1 August 2024; accepted 22 August 2024; published 6 September 2024)

The subtle interaction of low dimensionality and spin correlations in two-dimensional quantum magnets results in novel states of matter. Herein, we investigate the structural, magnetic, heat capacity, ^{31}P nuclear magnetic resonance (NMR) measurements, and density functional theory + Hubbard U (DFT + U) electronic structure calculations on the Cu^{2+} ($S = \frac{1}{2}$)-based compound $\text{BaCu}_2(\text{PO}_4)_2(\text{H}_2\text{O})$. Based on the hopping parameters obtained from DFT, the titled compound comprises the 2D layer of $1/3$ -depleted anisotropic kagome lattice with the magnetic couplings J_1 , J_2 , J_3 , and J_4 . At high temperatures, magnetic susceptibility (χ) exhibits paramagnetic behavior, with a Curie-Weiss temperature of $\theta_{\text{CW}} \approx -67$ K, indicating the presence of dominant antiferromagnetic interactions. The appearance of a broad maximum in the magnetic susceptibility and heat capacity reveals the low-dimensional nature of the compound. While the sharp magnetic anomaly features are not seen clearly in the bulk measurements, the ^{31}P NMR local probe measurements unambiguously show the presence of magnetic transition at $T_N = 10.5$ K. The temperature (T) dependence of nuclear spin-lattice relaxation rate ($1/T_1$) exhibits a sharp peak at T_N . While $1/T_1$ falls very steeply below T_N , it follows a sublinear power-law behavior above T_N , indicating the presence of dynamic short-range correlations, which could be attributed to the complex 2D spin network of the compound.

DOI: [10.1103/PhysRevB.110.125112](https://doi.org/10.1103/PhysRevB.110.125112)

I. INTRODUCTION

Quantum magnetism in low-dimensional systems is currently one of the captivating research fields offering a variety of rich quantum magnetic phenomena [1]. The diversity inherent in various spin-lattice models contributes to the emergence of intriguing and exotic quantum ground states. In recent years, low-dimensional $S = \frac{1}{2}$ systems have garnered significant attention due to the large quantum fluctuations. Among the plethora of 2D spin systems, the $S = \frac{1}{2}$ kagome-lattice antiferromagnets (KAFMs) provide a fascinating physical model, which piqued the curiosity of researchers. The reason lies in the interplay between robust quantum fluctuations and spin frustration, which results in the realization of a quantum spin-liquid (QSL) ground state featuring low-lying excitations with fractional quantum numbers [2–5]. Synthetic copper minerals such as $\text{ZnCu}_3(\text{OH})_6\text{Cl}_2$ stand out as exceptional material realization of an isotropic kagome lattice, representing a forefront in quantum magnetism research [6–12]. Even

though a QSL state is predicted in $\text{ZnCu}_3(\text{OH})_6\text{Cl}_2$ due to the absence of magnetic ordering down to 50 mK, there are still persistent debates revolving around its precise nature. It is unclear whether it is exhibiting a gapped or a gapless ground state [8,9]. The debate probably arises from the material's inherent complexity and a notable 5–10% disorder between Cu and Zn atoms [10–12]. It has been noticed that the real materials are typically afflicted by symmetry reduction from the ideal kagome structure due to the presence of the intense Jahn-Teller effect and significant Dzyaloshinskii-Moriya interactions, resulting in spatially anisotropic exchange interactions [13,14]. The lattice defects and the resulting perturbation terms are generally deleterious to quantum spin liquids. However, in some cases, the interaction of these defects and perturbations with geometric frustration can result in a slew of exotic quantum ground states [15].

A few known anisotropic kagome systems are $\text{Rb}_2\text{Cu}_3\text{SnF}_{12}$ [16–19], volborthite $\text{Cu}_3\text{V}_2\text{O}_7(\text{OH})_2 \cdot 2\text{H}_2\text{O}$ [20–22], vesignieite $\text{BaCu}_3\text{V}_2\text{O}_8(\text{OH})_2$ [23,24], and $\text{PbCu}_3\text{TeO}_7$ [25–27]. The compounds vesignieite and volborthite are magnetically ordered, whereas the compound $\text{Rb}_2\text{Cu}_3\text{SnF}_{12}$ has been laid out as a pinwheel valence bond solid with a spin gap of 20 K. On the other hand, the compound $\text{PbCu}_3\text{TeO}_7$, a deformed staircase kagome lattice,

*Contact author: ph20d504@iittp.ac.in

^{\dagger}These authors contributed equally to this work.

^{\ddagger}Contact author: koteswararao@iittp.ac.in

shows magnetic field-induced ferroelectricity [26]. While significant attention has been directed toward anisotropic kagome lattices in recent years, there has also been a rising curiosity regarding depleted 2D kagome systems [28–36]. For instance, the compound $\text{LiZn}_2\text{Mo}_3\text{O}_8$ with 1/3-filled or 2/3-depleted kagome lattice demonstrates quantum spin liquid behavior [30–32]. Conversely, 1/6-filled kagome magnet $\text{Li}_2\text{InMo}_3\text{O}_8$ exhibits the magnetic LRO [33–35]. Despite these advancements, there remains a gap in our understanding of depleted kagome variations. Herein, we come up with a novel quantum magnetic system $\text{BaCu}_2(\text{PO}_4)_2(\text{H}_2\text{O})$, which features a 2D layer comprising of 1/3-depleted anisotropic kagome lattice of Cu^{2+} ions with the magnetic couplings J_1 , J_2 , J_3 , and J_4 . We report the detailed investigation using nuclear magnetic resonance (NMR), magnetic susceptibility, heat capacity, and electronic band structure calculations of the compound $\text{BaCu}_2(\text{PO}_4)_2(\text{H}_2\text{O})$. The interaction between Cu^{2+} ions is antiferromagnetic (AFM), as evidenced by the Curie-Weiss temperature $\theta_{\text{CW}} \approx -67$ K obtained via magnetic susceptibility and ^{31}P NMR shift analysis. The unusual shape of the NMR spectrum might be an indication of incommensurate magnetic order. The nuclear spin-lattice relaxation rate ($1/T_1$) shows a prominent peak at $T_N = 10.5$ K. Above the critical temperature T_N the $1/T_1$ shows a sublinear power-law behavior. This suggests the existence of dynamic short-range correlations in the compound, likely originating from its intricate two-dimensional spin network.

II. TECHNIQUES

The synthesis of $\text{BaCu}_2(\text{PO}_4)_2(\text{H}_2\text{O})$ crystals were done using the one-pot hydrothermal technique. The high-purity chemicals of $\text{BaCl}_2 \cdot 2\text{H}_2\text{O}$ (Aldrich, 99.99%), $\text{CuCl}_2 \cdot 2\text{H}_2\text{O}$ (Aldrich, 99.99%), H_3PO_4 , and pyridine (0.5 ml) were taken in a stoichiometric proportion. The chemicals were further dissolved in 20 ml H_2O and mixed thoroughly for an hour before placing them in a 50 ml teflon-lined autoclave. The hydrothermal autoclave container was heated at 180°C for 72 hours and slowly cooled down with a ramp rate of $5^\circ/\text{hr}$. At room temperature, single crystal x-ray diffraction (XRD) was carried out on good quality single crystals utilizing a Bruker D8 Venture Diffractometer Dual Source (Mo,Cu). The data was acquired with APEX3 and reduced using SAINT/XPREP [37]. The structure was solved using direct approaches with SHELXT-2018/2 [38] and refined using complete matrix least squares on F2 with SHELXL-2018/3 [39]. To further ensure the single phase of the crystals, a significant number of single crystals were crushed into powder, and powder XRD measurements were done at room temperature using a PANalytical powder diffractometer with $\text{Cu} - K_\alpha$ radiation ($\lambda_{\text{avg}} \approx 1.54 \text{ \AA}$), which is consistent with the reported data [40,41]. Rietveld refinement analysis is done by using the FullProf Suite software package [42], giving out the goodness of fit value as 3.85 (see Fig. 1). The obtained lattice parameters from the refinement at room temperature are $a = 5.16 \text{ \AA}$, $b = 9.73 \text{ \AA}$, $c = 14.55 \text{ \AA}$, and $V = 731.09 \text{ \AA}^3$, which are in close agreement with the single-crystal XRD data. The heat capacity and magnetization measurements were performed by utilizing the heat capacity and vibrating-sample

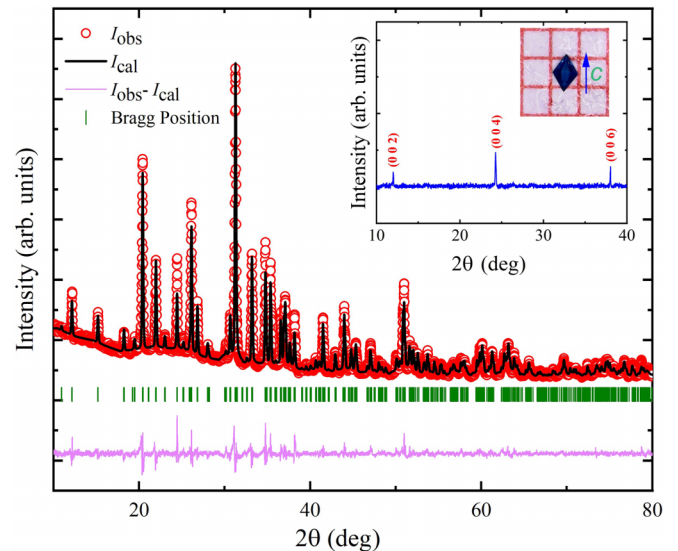


FIG. 1. Rietveld refinement of the XRD data at room temperature. The Bragg positions are shown with dark-green vertical bars, and the solid-pink line represents the difference between the experimental and calculated intensities. (Inset) The image of the grown $\text{BaCu}_2(\text{PO}_4)_2(\text{H}_2\text{O})$ single crystal with the XRD of (0 0 l) plane.

magnetometer options of a Quantum Design physical property measurement system, respectively. The phosphorus ^{31}P NMR experiments were carried out on Bruker AVANCE-II-360 NMR spectrometer at 8.5 T magnetic field using a home-built probe having a single-axis goniometer. A single crystal with dimensions of $1.2 \times 1.0 \times 0.6 \text{ mm}^3$ was used for the measurements. These measurements were conducted with the $\text{BaCu}_2(\text{PO}_4)_2(\text{H}_2\text{O})$ single crystal oriented in two directions, specifically with the external magnetic field aligned parallel to the c axis and parallel to the a axis. All the frequency shifts are given relative to the frequency of liquid H_3PO_4 reference at 145.53 MHz. The spin-lattice relaxation was measured using an inversion-recovery pulse sequence method.

III. RESULTS AND ANALYSIS

A. Crystal structure

The compound $\text{BaCu}_2(\text{PO}_4)_2(\text{H}_2\text{O})$ crystallizes in the orthorhombic space group $P2_12_12_1$ [40,41]. It lies in the Ba-Cu-P-O family system. The crystal structure is displayed in Fig. 2. The unit cell [see Fig. 2(a)] comprises two crystallographically distinct Cu atoms, which tend to form $\text{CuO}_4(\text{H}_2\text{O})$ square pyramids, and two crystallographically independent P atoms that are coupled tetrahedrally with four oxygen atoms to generate deformed PO_4 tetrahedra. The square pyramids of both Cu atoms form zigzag chains along the b axis that are interconnected to form a 2D-layered network of a 1/3-depleted kagome lattice [see Fig. 2(b)]. The interlayer separation is about 8.01 \AA . The anhydrous counterpart of the titled compound, $\text{BaCu}_2(\text{PO}_4)_2$, also exists within the Ba-Cu-P-O system. In this case, it features 1D antiferromagnetic (AFM) linear chains [43]. On the other hand, the compound $\text{BaCu}_2(\text{PO}_4)_2(\text{H}_2\text{O})$ manifests a 2D magnetic topology. The existence of 2D magnetic topology was also indicated by

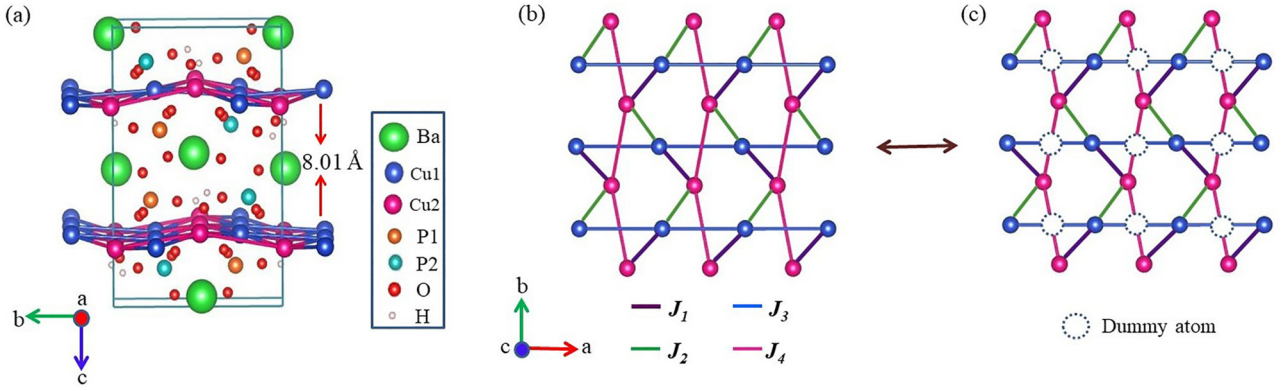


FIG. 2. (a) The unit-cell representation with an interlayer separation of about 8.01 Å for the compound BaCu₂(PO₄)₂(H₂O). (b) The spin network shows the 1/3-depleted anisotropic kagome lattice with J_1 , J_2 , J_3 , and J_4 couplings. (c) The 2D spin network with the dummy atoms reflects the 1/3-depleted anisotropic kagome lattice.

M. Yang [41] as models based on 1D AF Heisenberg chain and alternating spin chains failed to account for the observed magnetic behavior. The results obtained from DFT calculations indicate the presence of well-separated $S = \frac{1}{2}$ 2D layers, resembling a 1/3-depleted kagome lattice. A dummy atom has been intentionally added to the lattice to reflect a 1/3-depleted anisotropic kagome lattice in the BaCu₂(PO₄)₂(H₂O) system [see Fig. 2(c)]. This signifies a distinct magnetic structure compared to its anhydrous counterpart, showcasing the intriguing diversity within the Ba–Cu–P–O system. The bond path for J_1 and J_2 magnetic couplings is via O atoms, with the bond angles of Cu–O–Cu paths as 109.02° and 106.85°, respectively. The superexchange interaction paths with such bond angles favor weak AFM coupling as per the Goodenough-Kanamori rules [44]. In contrast, the magnetic couplings J_3 and J_4 are connected via longer paths Cu–O–P–O–Cu, which involve both O and P atoms, which is similar to the interaction paths for the compounds Ba₂Cu(PO₄)₂ and BaCuP₂O₇ [45]. The aforementioned interaction pathways in J_3 and J_4 couplings may account for their compatible magnetic interaction strength. The specifics of all the possible magnetic couplings for BaCu₂(PO₄)₂(H₂O) are summarized in Table I.

B. Magnetic susceptibility

Magnetization as a function of temperature from 2 K to 300 K is measured on a single crystal of BaCu₂(PO₄)₂(H₂O) in the presence of a magnetic field of 1 T parallel to the c axis as shown in Fig. 3(a). The inset of Fig. 3(a) presents the magnetic data at 0.1 T for the crystallographic directions a , b , and c , whereas the inset of Fig. 3(b) illustrates the data at 0.5 T. It is evident that the $\chi(T)$ data for $H_{\text{ext}}//a$ is different

from that of $H_{\text{ext}}//b$, which is probably due to the presence of in-plane anisotropy within the 2D lattice (ab plane). The ab -plane anisotropy is due to the complex nature of anisotropic exchange interactions and the depleted nature of 2D lattice unlike that of a perfect 2D kagome lattice where the $\chi(T)$ for $H_{\text{ext}}//a$ and $H_{\text{ext}}//b$ directions are expected to be the same. It is to be noted that there is a very small upturn (Curie behavior) noticed in the $\chi(T)$ data along the a axis at 0.1 T, which can be attributed to the presence of small paramagnetic impurities in the system. The presence of a broad maximum in $\chi(T)$ at 25 K is a defining property of low-dimensional quantum magnetic systems. Figure 3(b) represents the temperature-dependent inverse magnetic susceptibility $1/\chi$ of the sample BaCu₂(PO₄)₂(H₂O). In the temperature range 70–300 K, the $1/\chi$ values are fitted using the Curie-Weiss (CW) law,

$$\chi = \chi_o + \frac{C}{T - \theta_{\text{CW}}} \quad (1)$$

where C denotes the Curie constant, χ_o represents the temperature-independent susceptibility, and θ_{CW} denotes the CW temperature.

The parameters obtained from the CW fit are $\chi_o \simeq -8.57 \times 10^{-5} \text{ cm}^3/\text{mol-Cu}$, which is the sum of core diamagnetic susceptibility (χ_{dia}) and Van-Vleck susceptibility (χ_{VV}), $C \simeq 0.47 \text{ cm}^3\text{K}/\text{mol-Cu}$, and $\theta_{\text{CW}} \simeq -67 \text{ K}$. A negative value of θ_{CW} implies that the dominant interactions between Cu²⁺ ions are AFM in nature. The diamagnetic susceptibility of BaCu₂(PO₄)₂(H₂O) was determined to be $\simeq -1.64 \times 10^{-4} \text{ cm}^3/\text{mol-Cu}$ by adding the core diamagnetic susceptibilities of individual ions Ba²⁺, Cu²⁺, P⁵⁺, H⁺ and O²⁻ [46]. Subtracting χ_{dia} from χ_o yields the paramagnetic susceptibility χ_{VV} , which is determined to be $\simeq 7.83 \times$

TABLE I. The details of the bond path, bond length, and bond angle of the magnetic couplings for BaCu₂(PO₄)₂(H₂O).

Coupling	Bond path	Bond length (Å)	Bond angle (°)
J_1	Cu1-O4-Cu2	3.25	Cu1-O4-Cu2 = 109.02
J_2	Cu2-O5-Cu1	3.19	Cu2-O5-Cu1 = 106.85
J_3	Cu1-O1-P1-O4-Cu1	5.16	Cu1-O1-P1 = 130.24 P1-O4-Cu1 = 121.22
J_4	Cu2-O2-P1-O4-Cu2	5.05	Cu2-O2-P1 = 129.56 P1-O4-Cu2 = 121.03

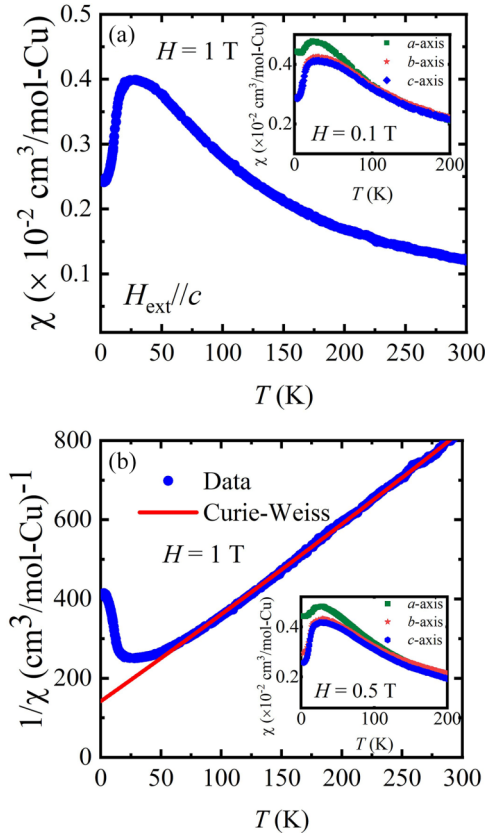


FIG. 3. (a) The measured magnetic susceptibility χ data as a function of T in an applied field of 1 T. (Inset) The $\chi(T)$ data at 0.1 T for different crystallographic directions. (b) The inverse magnetic susceptibility $1/\chi$ vs T . The solid-red line indicates the fit to the Curie-Weiss law. (Inset) The $\chi(T)$ data at 0.5 T for different crystallographic directions.

$10^{-5} \text{ cm}^3/\text{mol-Cu}$, arising from the magnetic field's second-order contribution to free energy. Assuming a Landé g factor of 2, the spin-only effective moment for an $S = 1/2$ system is $\mu_{\text{eff}} = g\sqrt{S(S+1)}\mu_B \approx 1.73\mu_B$, where μ_B is the Bohr magneton. However, our experimental value of the spin-only effective moment is $\mu_{\text{eff}} \approx 1.94\mu_B$, which is determined using the Curie constant value by utilizing the relation $\mu_{\text{eff}} = \sqrt{3k_B C/N_A} \approx \sqrt{8C}\mu_B$, where N_A is Avogadro's number and k_B is the Boltzmann constant. Due to the unquenched spin-orbit coupling, this value of μ_{eff} is somewhat bigger than the value of $1.73\mu_B$ for free $S = 1/2$ and has been observed in various Cu^{2+} -based compounds [47,48].

C. Heat capacity

The temperature-dependent heat capacity $C_p(T)$ is measured at zero field, as shown in Fig. 4(a). At higher temperatures, C_p in magnetic insulators often contribute significantly to phonon excitations C_{ph} . However, in contrast, when we proceed to lower temperatures, the magnetic part of the heat capacity C_m takes precedence over C_{ph} . As a result, in magnetic systems with a low-energy scale of exchange coupling, the magnetic and phononic parts can be distinguished by evaluating C_p in the high-temperature region. The phonon contribution was initially estimated to extract C_m from C_p

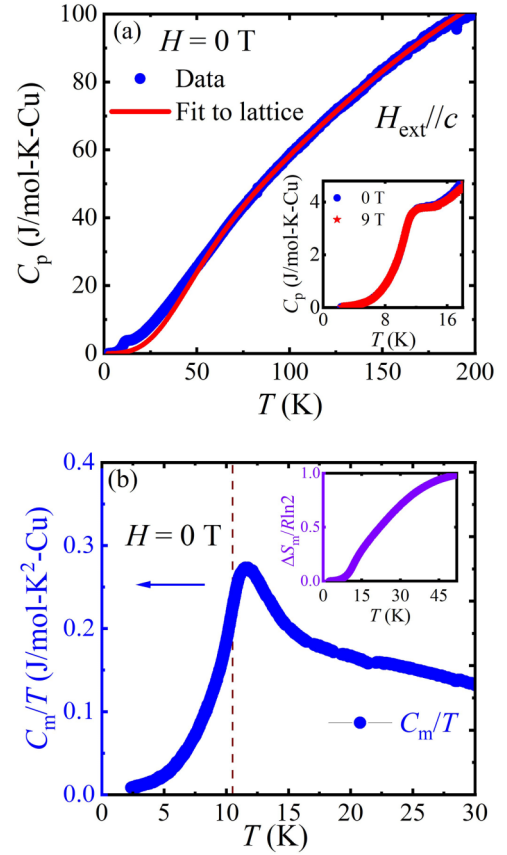


FIG. 4. (a) Variation of heat capacity (C_p) with respect to the T in zero field. The solid-red line reflects the phononic contribution (C_{ph}). (Inset) Temperature variation of C_p at 0 T and 9 T. (b) Plot of C_m/T vs T , the dashed vertical-brown line represents the magnetic transition $T_N = 10.5$ K obtained from the NMR measurement. (Inset) Variation of normalized magnetic entropy $\Delta S_m/R\ln 2$ with respect to the T .

by fitting the high- T data with one Debye and two Einstein terms [49],

$$C_{\text{ph}}(T) = f_D C_D(\theta_D, T) + \sum_{i=1}^2 g_i C_{E_i}(\theta_{E_i}, T). \quad (2)$$

The first term in Eq. (2) represents the Debye model,

$$C_D(\theta_D, T) = 9nR \left(\frac{T}{\theta_D} \right)^3 \int_0^{\theta_D/T} \frac{x^4 e^x}{(e^x - 1)^2} dx, \quad (3)$$

where $x = \frac{\hbar\omega}{k_B T}$, ω is the Debye frequency, R is the universal gas constant, and θ_D represents the Debye temperature. The second part in Eq. (2) is known as the Einstein term, which accounts for the flat optical modes of the lattice vibrations,

$$C_E(\theta_E, T) = 3nR \left(\frac{\theta_E}{T} \right)^2 \frac{e^{\theta_E/T}}{[e^{\theta_E/T} - 1]^2}. \quad (4)$$

The characteristic Einstein temperature is represented by θ_E . The coefficients f_D and g_1 , and g_2 are weight factors that take the number of atoms per formula unit (n) into consideration.

The zero fields $C_p(T)$ data above 55 K are fitted with a linear combination of one Debye and two Einstein parameters

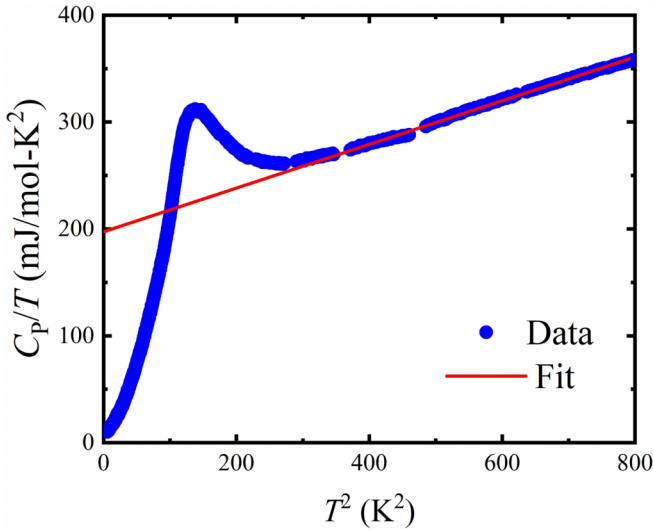


FIG. 5. The plot of C_p/T vs T^2 with fit (red line) to the linear equation from 20 K to 28 K. The fit is further extrapolated to the low temperatures.

using Eq. (2) [see the solid-red curve in Fig. 4(a)], and the obtained parameters are $f_D \approx 0.19 \pm 0.05$, $g_1 \approx 0.28 \pm 0.05$, $g_2 \approx 0.42 \pm 0.05$, $\theta_D \approx 277 \pm 2$ K, $\theta_{E1} \approx 689 \pm 2$ K, and $\theta_{E2} \approx 1104 \pm 3$ K. The C_p data, depicted in Fig. 4(a), exhibits a broad shoulder at a temperature of 12 K. It has been noticed in many low dimensional magnetic materials that the broad shoulder in C_p occurs at lower temperatures when compared with the broad maximum in the χ data [47,50]. The inset of Fig. 4(a) depicts the $C_p(T)$ measured in the applied field of 9 T in the low-temperature regime. A field change from 0 to 9 T produces no noticeable difference. The C_m was finally calculated by extrapolating the high- T fit down to 2 K and subtracting it from the measured C_p data,

$$S_m = \int \frac{C_m(T)}{T} dT. \quad (5)$$

The change in magnetic entropy ΔS_m is further estimated by integrating the calculated $\frac{C_m(T)}{T}$ data using Eq. (5). The obtained value of ΔS_m saturates above 55 K [see inset of Fig. 4(b)]. It approaches a value of 5.73 J/mol-K. This value is in good agreement with the theoretically predicted value 5.75 J/mol-K for an $S = 1/2$ system. In the following section, we use nuclear magnetic resonance to investigate the static and dynamic spin characteristics of the compound $\text{BaCu}_2(\text{PO}_4)_2(\text{H}_2\text{O})$.

To gain further insight, we plotted the heat capacity divided by temperature, C_p/T , against T^2 for $\text{BaCu}_2(\text{PO}_4)_2(\text{H}_2\text{O})$, as shown in Fig. 5. The solid-red line represents a fit to the linear equation in the temperature range of $400 < T^2 < 800$ ($20 \text{ K} < T < 28 \text{ K}$). The yielded value of the intercept is $197 \text{ mJ/molK}^2\text{-Cu}$. This linear contribution to the heat capacity has been noticed in a few 2D spin-liquid-like candidates of different topologies [51,52] and quasi-1D chains exhibiting the Luttinger liquid-like excitations (dimensional reduction due to high frustration) [53,54]. However, a thorough investigation using local probe techniques such as inelastic neutron

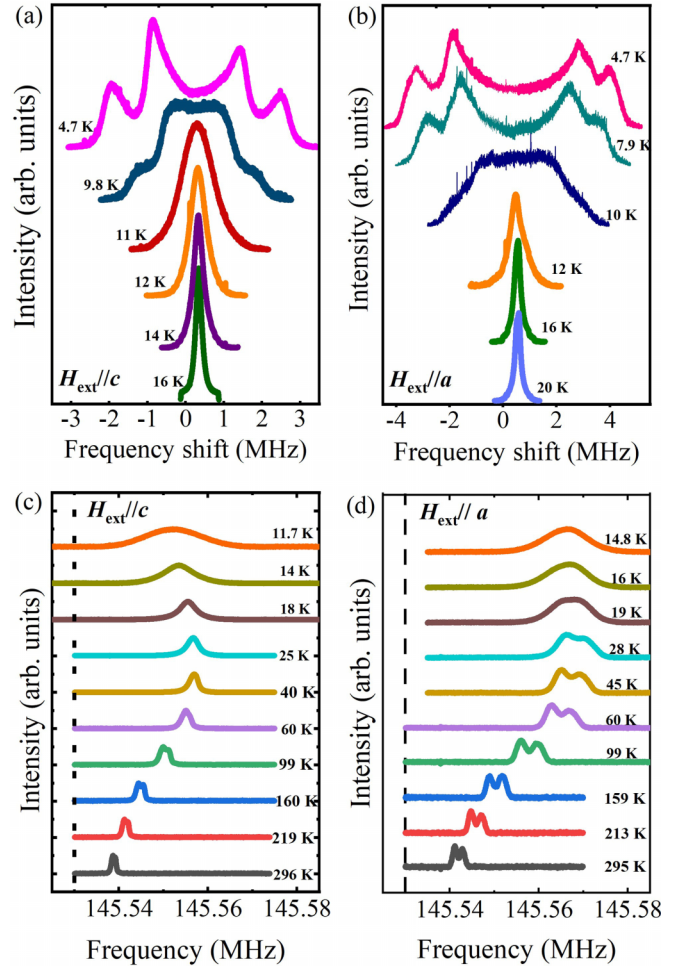


FIG. 6. The ^{31}P NMR spectra of $\text{BaCu}_2(\text{PO}_4)_2(\text{H}_2\text{O})$ in two orthogonal orientations ($H_{\text{ext}}//c$ and $H_{\text{ext}}//a$) of a single crystal in 8.5 T fixed magnetic field. The low-temperature NMR spectra is shown in (a) and (b), and the spectrum at higher temperatures is shown in (c) and (d). The vertical dash-dotted line in (c) and (d) represent the reference frequency using liquid H_3PO_4 , which also has a zero shift of the ^{31}P nucleus.

scattering (INS) is further warranted to get proper insights on the excitations of the system [55,56].

D. ³¹P NMR

1. NMR spectrum

Nuclear magnetic resonance (NMR) is a powerful local probe tool used to analyze the static and dynamic characteristics of quantum spin systems. It has been widely employed to examine diverse low-dimensional quantum magnetic systems. Figure 6 depicts the temperature dependence of the ^{31}P ($I = \frac{1}{2}$) NMR spectra measured on a single crystal with the size $1.2 \times 1.0 \times 0.6 \text{ mm}^3$ at a fixed magnetic field of 8.5 T. The observed spectra exhibit a characteristic anisotropic pattern shape. The spectra become broader and shift as the temperature decreases. The NMR spectra of the titled compound at high temperatures consist of two resonance spectral lines (see Fig. 6), which are very close to each other. This further

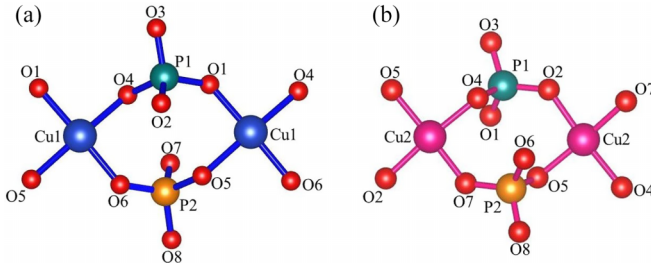


FIG. 7. The environment of P1 and P2 sites with respect to the Cu1 and Cu2 atoms, respectively.

suggests that $\text{BaCu}_2(\text{PO}_4)_2(\text{H}_2\text{O})$ contains two nonidentical ^{31}P sites.

The pictorial representation of the P1 and P2 atom's environment is shown in Fig. 7. The bond angle related to the P1 atom site concerning the Cu1 atom ($\text{O4-P1-O1} = 106.88^\circ$, $\text{P1-O4-Cu1} = 121.22^\circ$) is less than that of the P2 atom ($\text{O6-P2-O5} = 107.26^\circ$, $\text{P2-O6-Cu1} = 133.01^\circ$). A similar variation in bond angles ($\text{O4-P1-O2} = 108.26^\circ$, $\text{P1-O4-Cu2} = 121.02^\circ$, $\text{O7-P2-O5} = 106.51^\circ$, $\text{P2-O5-Cu2} = 115.40^\circ$) has been observed between the P1 and P2 atom sites relative to the Cu2. This indicates that the environments surrounding the two phosphorus atoms are somewhat distinct. Additionally, we have shown the high-resolution magic angle spinning (MAS) NMR spectrum in the Appendix (see Fig. 14 below). The temperature dependence of the ^{31}P NMR line shape at low temperatures in two different orientations is shown in Figs. 6(a) and 6(b). The line width grows gradually with decreasing temperature. Below 10.5 K, the line shape shows a pattern related to the distribution of the internal magnetic field at the ^{31}P sites due to the onset of incommensurate magnetic transition (T_N).

It is to be noted that we did not observe apparent features of any magnetic anomaly at 10.5 K in the $\chi(T)$ and $C_p(T)$ data. The presence of quantum fluctuations might be the reason for not noticing the magnetic anomaly at $T_N = 10.5$ K. In addition, in the C_p data, we did observe a broad shoulder at 12 K, which is close to the transition temperature; it must be ascribed to both influenced by short-range spin correlations and long-range order.

At 4.7 K, the NMR spectra exhibit a broad four-peak feature. Since we have two ^{31}P sites, one double-peak might be associated with each ^{31}P site. The double-peak or double-horn line shape is possibly due to the harmonic space variation of the resonant field (frequency) around the Zeeman value H_0 [57]. Similar characteristic line shapes and local field distribution have been reported earlier in the incommensurate phase of the low-dimensional magnetic compounds [57,58]. The description of the ^{31}P NMR line shape in the incommensurate AF phase is to assume different patterns for phosphorus P1 and P2 sites. For both phosphorus, one has a harmonic distribution of the local field at the phosphorus site i counting the position related to the incommensurate order [59]:

$$H_{\text{loc}}^i = H_{\text{ext}} + H_0 + H_{\text{int}} \cos \theta_i, \quad 0 \leq \theta_i \leq 2\pi, \quad (6)$$

where $H_{\text{int}} = H_{hf} + H_{\text{dip}}$, the H_{dip} term signifies the contribution from the dipolar interactions, $H_{\text{ext}} = 8.5$ T is the external magnetic field, H_0 is a constant hyperfine field

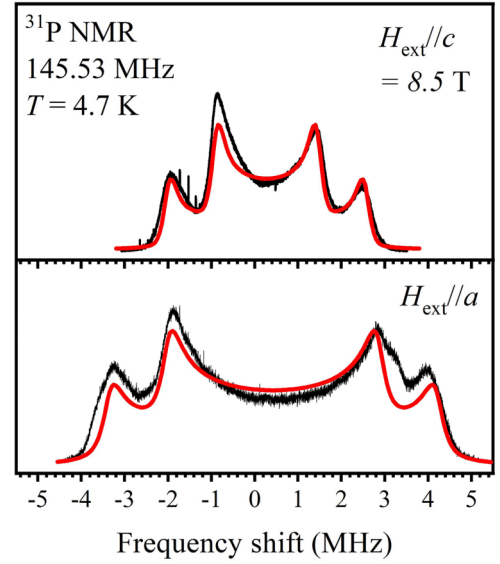


FIG. 8. Simulation (the red lines) of the local field distribution at phosphorus sites in two directions of the external magnetic field.

projection, and $H_{\text{int}} \cos \theta_i$ is the local field value at the phosphorus site i . The simulation of the local field distribution in the incommensurate AFM phase at phosphorus sites in two directions of the external magnetic field at 4.7 K is shown in Fig. 8. The incommensurate AFM order may be built by the amplitude modulation of the localized magnetic moments or by the helical order of local moments. The incommensurate phase featuring amplitude modulation has been observed as an intermediate phase in the one-dimensional system (TiPO_4) during the transition from a paramagnetic state to a dimerized singlet state [58]. In this case, one expects the parameter H_0 to vanish in all orientations. However, for our system, we have different H_0 values in $H_{\text{ext}} // c$ and $H_{\text{ext}} // a$, thus we believe that in the current case we have incommensurate AFM state with the helical arrangement of spin orientations. It is interesting to note that the local arrangement of PO_4 tetrahedra between corner shared CuO_4 plaquettes is similar to that in the structure of well-studied square cupola compound $\text{Ba}(\text{TiO})\text{Cu}_4(\text{PO}_4)_4$ [60] having perfect AFM ordering below $T_N = 9.5$ K. In the latter compound, the magnetic moments of copper are oriented perpendicular to the CuO_4 plaques, and the internal field at phosphorus nuclei is $H_{\text{int}} = 35.6$ mT [61], which is several times smaller compared to the internal field values for our compound as given in Table II.

TABLE II. Simulation parameters for the local field distribution in the incommensurate AFM phase.

	H_0		H_{int}	
	$H_{\text{ext}} // c$	$H_{\text{ext}} // a$	$H_{\text{ext}} // c$	$H_{\text{ext}} // a$
P1	300 kHz 17 mT	450 kHz 26 mT	2300 kHz 133 mT	3800 kHz 220 mT
P2	300 kHz 17 mT	450 kHz 26 mT	1200 kHz 70 mT	2450 kHz 142 mT

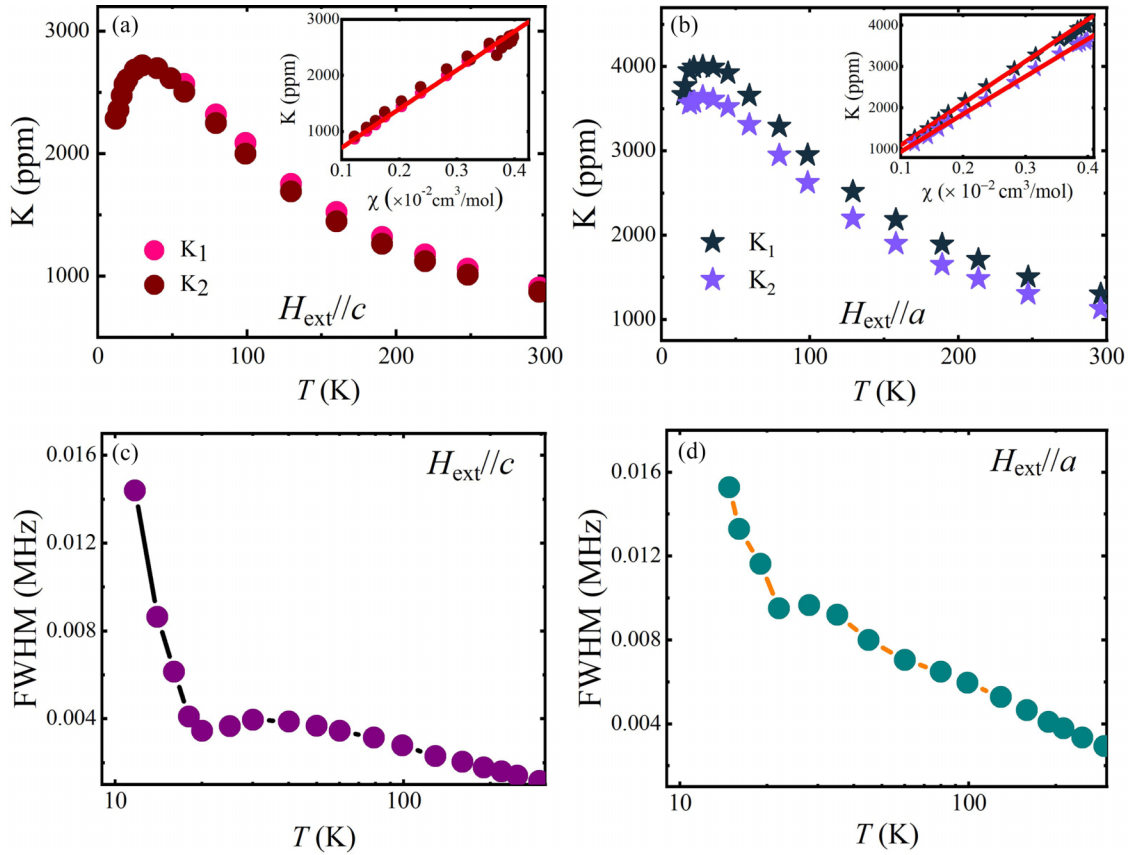


FIG. 9. The plot of NMR shift (K) vs T for ^{31}P nuclei in the direction $H_{\text{ext}}//c$ and $H_{\text{ext}}//a$ of the single crystal is shown in (a) and (b). The K_1 and K_2 represent the Knight shifts of P1 and P2 NMR lines. (Inset) K vs $\chi(T)$ in the T range 2–300 K for both orientations. The solid red line represents the linear fit. The full width at half maximum (FWHM) vs T plot for $H_{\text{ext}}//c$ and $H_{\text{ext}}//a$ direction is shown in (c) and (d).

2. K-Shift and FWHM

The NMR technique has a significant advantage over bulk susceptibility in determining intrinsic magnetism. In this technique, if present, the paramagnetic impurity contributions would broaden the NMR line but will not contribute to the central line of the NMR shift. As a result, obtaining the intrinsic $\chi_{\text{spin}}(T)$ from the temperature dependence of the $K(T)$ rather than the bulk susceptibility is more credible. In this compound, the PO_4 tetrahedrons at both sites (P1 and P2) are connected to the four nearest Cu^{2+} ions via hyperfine interaction.

The $K(T)$ can be expressed in terms of $\chi_{\text{spin}}(T)$ as

$$K(T) = K_0 + \frac{A_{\text{hf}}}{N_A \mu_B} \chi_{\text{spin}} \quad (7)$$

where K_0 denotes the temperature-independent chemical shift and $^{31}\text{A}_{\text{hf}}$ denotes the average hyperfine coupling between the ^{31}P nucleus and Cu^{2+} ions. Figures 9(a) and 9(b) depict $K(T)$ as a function of T for $H_{\text{ext}}//c$ and $H_{\text{ext}}//a$ direction of the single crystal. The $\chi_{\text{spin}}(T)$ is taken from Fig. 3(a).

The sample has a broad maximum at 25 K, confirming the presence of short-range correlations. The inset of Figs. 9(a) and 9(b) show the plot between $K(T)$ and $\chi(T)$ with a linear

fit. The plot demonstrates linear behavior across the whole temperature range. It is to be noted that the K_1 and K_2 are related to the P1 and P2 NMR lines. The knight shift values for P1 and P2 atoms show slight variation for $H_{\text{ext}}//a$, possibly due to the difference in the connectivity of the P1 and P2 atom (see Table I). The values of A_{hf} and K_0 are extracted from the slope of the linear fit for both orientations. The values obtained for the $H_{\text{ext}}//c$ orientation comes out to be (3.81 ± 0.02) kOe/ μ_B , (34.29 ± 2) ppm for K_1 and (3.85 ± 0.02) kOe/ μ_B , (36.62 ± 2) ppm for K_2 . Similarly, for the $H_{\text{ext}}//a$ orientation the values comes out to be (5.04 ± 0.02) kOe/ μ_B , (36.58 ± 2) ppm for K_1 and (5.63 ± 0.02) kOe/ μ_B , (48.35 ± 2) ppm for K_2 . Further, the amplitude of the hyperfine field (Table II) and the obtained average coupling constant were used to calculate the ordered moment for both the orientations of the crystal. For $H_{\text{ext}}//c$, the average ordered moment comes out to be $0.35 \mu_B$, whereas for $H_{\text{ext}}//a$ it comes out to be $0.42 \mu_B$. The NMR spectral data for both orientations, with the external magnetic field aligned parallel to the c axis and parallel to the a axis, were analyzed using suitable Gaussian fits to determine the full width at half-maximum (FWHM) values. The FWHM of the ^{31}P NMR spectra as a function of T is shown in Figs. 9(c) and 9(d). It displays a broad maximum at around 25 K, suggesting that FWHM traces the bulk $\chi(T)$, as expected. However, a notable increase in the FWHM below 20 K was observed, which could possibly be

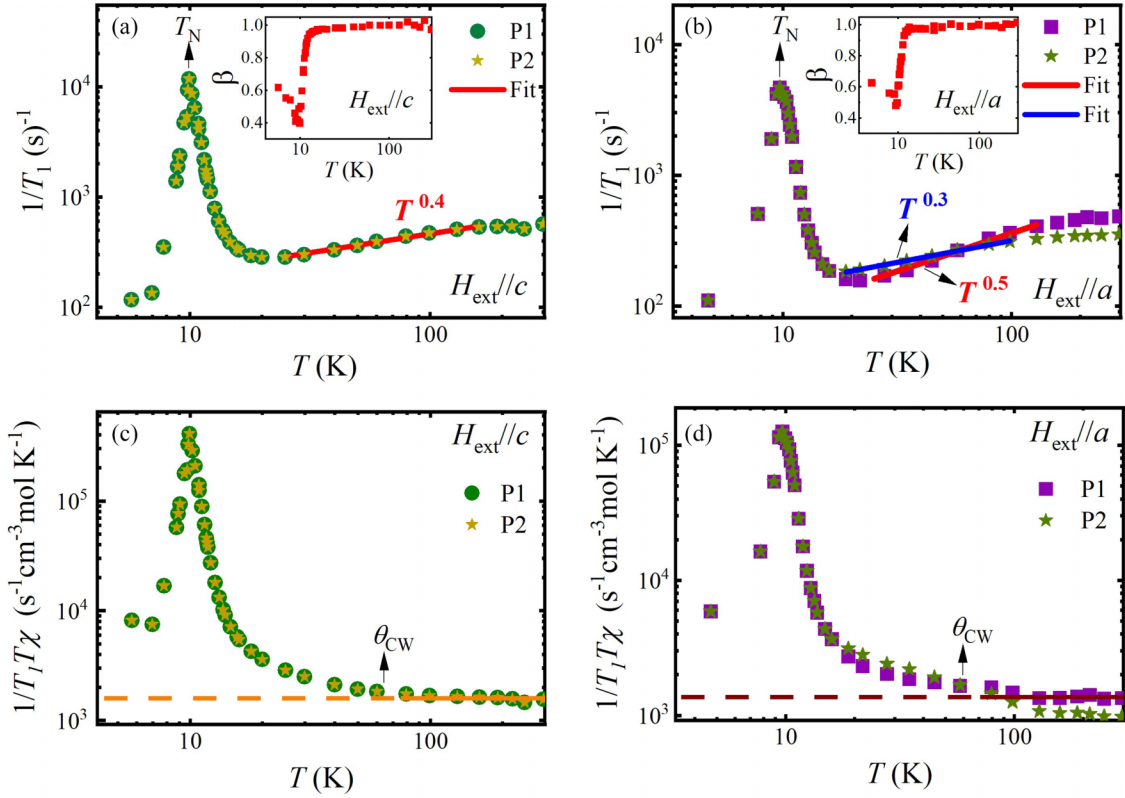


FIG. 10. Plot of spin-lattice relaxation rate $1/T_1$ as a function of T for ^{31}P nuclei in $H_{\text{ext}}//c$ and $H_{\text{ext}}//a$ direction is shown in (a) and (b). The solid-red lines represent the power-law fit. The temperature dependence of $1/T_1 T \chi$ for both the orientations is shown in (c) and (d). The inset in (a) and (b) shows the variation of the stretched parameter with temperature.

due to the development of an internal field as we approached the magnetic ordering temperature (T_N).

3. Spin-lattice relaxation

To investigate the microscopic properties of 2D Heisenberg antiferromagnets, it is necessary to measure the temperature dependence of the spin-lattice relaxation rate $1/T_1$, which provides information about the imaginary component of the dynamic susceptibility $\chi(q, \omega)$. The spin-lattice relaxation for the single crystal was measured for $H_{\text{ext}}//c$ and $H_{\text{ext}}//a$ directions using an inversion-recovery method. The $1/T_1$ at each temperature was determined by fitting the nuclear magnetization $M(t)$ versus time t using the single or stretched exponential recovery function,

$$M(t) = M_{\text{eq}} - M_0 \exp\left[-\left(\frac{t}{T_1}\right)^\beta\right]. \quad (8)$$

The stretched exponent β provides the inhomogeneous distribution of $1/T_1$. When the value of β becomes 1, then Eq. (8) simplifies to a single exponential function, which accounts for the homogenous relaxation. Near or below T_N , $1/T_1$ was measured at the center of the broad NMR spectra to avoid losing the intrinsic nature of the distribution of hyperfine fields [59]. Figures 10(a) and 10(b) depict the temperature dependence of $1/T_1$ for ^{31}P nuclei in $H_{\text{ext}}//c$ and $H_{\text{ext}}//a$ direction with a sharp peak at 10.5 K, confirming the presence of magnetic LRO ($T_N = 10.5$ K). The $1/T_1$ data in the case

of $H_{\text{ext}}//c$ is same for both P1 and P2 atoms, whereas for $H_{\text{ext}}//a$ there is a small change in the slope above T_N . To understand the behavior of spins above T_N , the spin-lattice relaxation data for both orientations is fitted with a power law for varying temperature ranges. The data aligns well with power-law behavior, yielding an exponent of 0.4 for $H_{\text{ext}}//c$, with the data for P1 and P2 atoms overlapping as anticipated for spin-lattice relaxation. However, for $H_{\text{ext}}//a$, we observe two distinct power laws (0.5 and 0.3) for P1 and P2 atoms. This may be attributed to slight environmental changes related to the phosphorous atoms, which are also evident in the Knight shift data. This sublinear behavior in both orientations of the single crystal indicates the appearance of short-range spin correlations [62]. As the temperature dropped further, a sharp anomaly was seen at $T_N = 10.5$ K due to the crucial slowing down of fluctuating moments. As the critical fluctuations and variations in the ordered state disappear below T_N , $1/T_1$ rapidly declines toward zero. The temperature dependence of the stretch exponent is illustrated in the inset of Figs. 10(a) and 10(b). Above T_N , recovery curves conform well to a single exponential function. However, below T_N , a stretched exponential function was necessary. This is probably due to the distribution of hyperfine fields resulting from the incommensurate spin ordering below T_N . Finally, to examine the impact of spin fluctuation in the paramagnetic state above T_N , we replotted the data by switching the vertical axis from $1/T_1$ to $1/T_1 T \chi$ [see Figs. 10(c) and 10(d)]. There is a direct relationship between $1/T_1 T$ and the imaginary part of the dynamic susceptibility $\chi''(q, \omega_N)$, where ω_N is the NMR

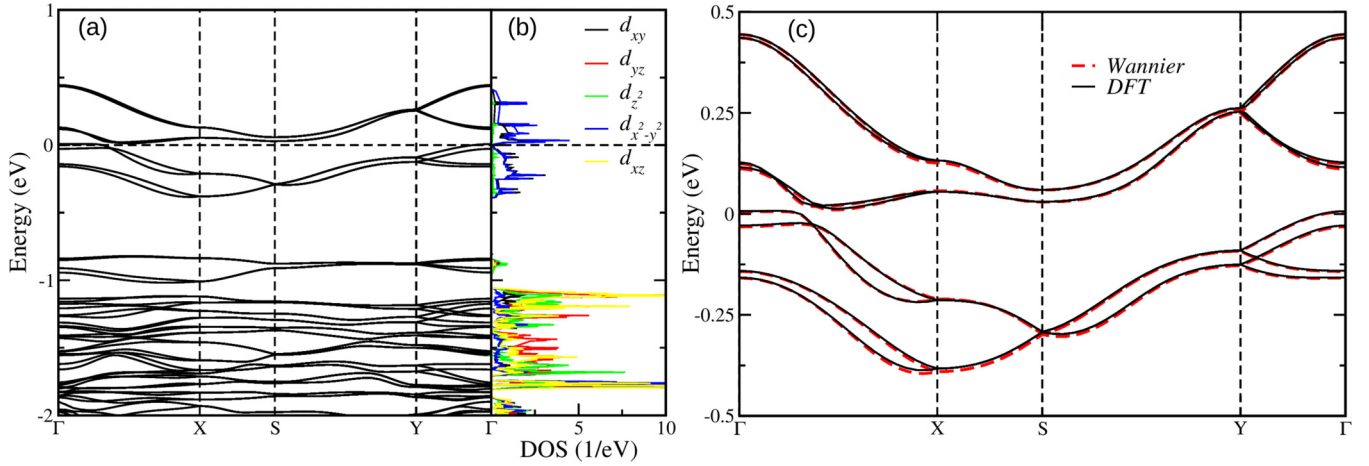


FIG. 11. Nonspin polarised band dispersion along high-symmetry k points in the first Brillouin zone. (b) Orbital-resolved PDOS with dominating $d_{x^2-y^2}$ character at the Fermi level. (c) Wannier interpolated bands on top of DFT bands.

frequency [63],

$$\frac{1}{T_1 T} = \frac{2\gamma_N^2 k_B}{N_A^2} \sum_q |A(q)|^2 \frac{\chi''(q, \omega_N)}{\omega_N} \quad (9)$$

where k_B is Boltzmann's constant. The summation is over the wave vectors q within the first Brillouin zone in the preceding equation, and $A(q)$ represents the form factor of the hyperfine interactions. The real part of $\chi'(q, \omega_N)$ is the uniform static susceptibility $\chi = \chi'(0, 0)$, where both $q = 0$ and $\omega_N = 0$. Consequently, by plotting $1/T_1 T \chi$ vs T , we can relate the temperature dependency of $\sum_q |A(q)|^2 \chi''(q, \omega_N)$ with the uniform susceptibility $\chi'(0, 0)$. In the high-temperature zone $T > \theta_{CW}$, $1/T_1 T \chi$ is almost temperature independent, as seen in Figs. 10(c) and 10(d). This suggests that at higher temperatures (above 80 K), the term $\sum_q |A(q)|^2 \chi''(q, \omega_N)$ scales down to $\chi'(0, 0)$. On the other hand, when we further go down below θ_{CW} , it increases with the decrease in temperature, which suggests that the term $\sum_q |A(q)|^2 \chi''(q, \omega_N)$ increase more rapidly than $\chi'(0, 0)$. This finding shows an increase in spin fluctuations with $q \neq 0$, which can be attributed to the presence of AFM correlations.

E. Electronic structure calculations

In order to understand the ground state electronic structure of $\text{BaCu}_2(\text{PO}_4)_2(\text{H}_2\text{O})$, density functional theory (DFT) calculations are carried out using Vienna *ab initio* simulation package (VASP) [64,65] where wavefunctions are expanded in plane wave basis sets. Exchange and correlation effects are treated within the generalized gradient approximation (GGA) of Perdew-Burke-Ernzerhof [66]. Further, to account for the correlation effects of Cu d -orbitals, Hubbard $U = 6$ eV is included in the GGA+ U framework.

The choice of U is made based on the previous studies on Cu-based systems [67,68]. The kinetic energy cut-off is set at 500 eV. The Brillouin zone integration for a $4 \times 3 \times 4$ k mesh is performed using the tetrahedron method of Blöchl [69]. We calculated the intersite exchange parameters using the hopping parameters approach to understand the magnetism in detail. Here, hopping parameters are calculated upto the fourth

NN by constructing maximally localised wannier functions as suggested by Marzari and Vanderbilt [70]. These wannier functions are constructed from the random initial projections for bands dispersed near the Fermi level using the wannier90 package [71] in a nonspin polarised setup. First, we examined the nonspin polarised band dispersion along a high-symmetry k -path in the first Brillouin zone of the orthorhombic lattice, as shown in Fig. 11(a). The most striking feature of this band dispersion is the appearance of a total of eight bands around the Fermi level arising from the eight Cu ions in the unit cell. Further, our orbital resolved partial density of states corresponding to the Cu- d orbitals [Fig. 11(b)] reveals that these bands have predominantly $d_{x^2-y^2}$ characters, and they are just half-filled.

This basic electronic structure is consistent with the ligand field and +2 nominal charge state of Cu ions in this compound. The Cu ions being in the square pyramid environment of the O atoms and having a d^9 nominal occupation (+2 charge state), we observe a half-filled $d_{x^2-y^2}$ -states in the pure band theory. We will later show that these half-filled bands will give rise to an insulating ground state due to the presence of a strong electronic correlation (local Coulomb interaction term U), as expected from the solution of the Hubbard model. Since the low-energy physics of this materials is arising from these $d_{x^2-y^2}$ bands around the Fermi energy, and they are well separated from the rest of the bands, we constructed effective Wannier orbitals using wannier90 formalism [71]. The superposition of interpolated Wannier bands on top of the DFT bands is displayed in Fig. 11(c). This procedure provides us the effective inter-atomic hopping parameters t_n in a low-energy tight-binding model where Cu- $d_{x^2-y^2}$ is the only active orbital, and all the other orbitals are downfolded. The computed t_n for various Cu-Cu distances are shown in Table III. In the limit of high U values, we can map the Hubbard model to a Heisenberg model where antiferromagnetic coupling between Cu ions can be expressed as $J_n = \frac{4t_n^2}{U}$. Hence, we computed the strength of relative magnetic coupling (antiferromagnetic) between the nearest-neighbor Cu ions, as shown in Table III. We note that this method has been widely employed for determining inter-atomic magnetic interactions [72,73]. These values

TABLE III. The relative magnetic exchange interactions between Cu^{2+} ions extracted from the hopping parameters of the 2D magnetic layer.

Hopping	Hopping parameters (meV)	$\frac{J_i}{J_1} = \left(\frac{t_i}{t_1}\right)^2$
t_1	120.13	1.00
t_2	93.98	0.60
t_3	91.56	0.58
t_4	76.95	0.41

of the exchange couplings show that the titled compound has four dominant couplings in the 2D magnetic layer, namely J_1 , J_2 , J_3 , and J_4 [see Fig. 2(b)]. The strength of the J_1 coupling is the strongest, whereas the relative magnetic strengths of the other three couplings are comparable with each other. Hence, the spin network of $\text{BaCu}_2(\text{PO}_4)_2(\text{H}_2\text{O})$ can be considered a 1/3-depleted anisotropic 2D kagome lattice, which has a reduced magnetic frustration compared to the perfect 2D kagome lattice. Next, we examined the relative stability of various magnetic states within the GGA+ U approach. The obtained energies for configuration 1, configuration 2, and configuration 3 are (0.0 meV/f.u.), (-8.38 meV/f.u.), and (-15.57 meV/f.u.). We can see that configuration-3 is lowest in energy where all four (first, second, third, and fourth NNs) Cu spins are coupled antiferromagnetically (see Fig. 12). This is consistent with our computed antiferromagnetic interaction, as discussed above.

We finally discussed the electronic structure in the lowest-energy magnetic state obtained from our calculations. Figure 13 shows the computed total and partial densities of states (DOS) for the Cu- d and O- p states. The total DOS [Fig. 13(a)] clearly illustrates that the ground state is insulating with a band gap of 1.85 eV. To further grasp the true nature of the insulating ground state, we analyze the projected DOS around the Fermi level. It can be clearly seen that the Cu- d majority spin channel [Fig. 13(b)] is fully occupied. However, the minority channel is partially filled with a small spectral weight above Fermi energy corresponding to the one hole in the d -spectral function. This arrangement of d states around the Fermi level in the magnetic state and an insulating ground state in the presence of strong electronic correlation is consistent with the Hubbard model physics, as discussed above. The magnetic moment at the Cu^{2+} site is estimated to be $0.72 \mu_B$, which is slightly less than the expected magnetic moment in nominal $3d^9$ configurations. This quenching of magnetic moment on the Cu site can be attributed to the hybridization

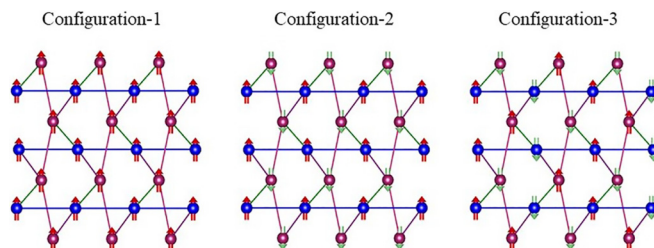


FIG. 12. Different magnetic configurations for estimating the lowest-energy state.

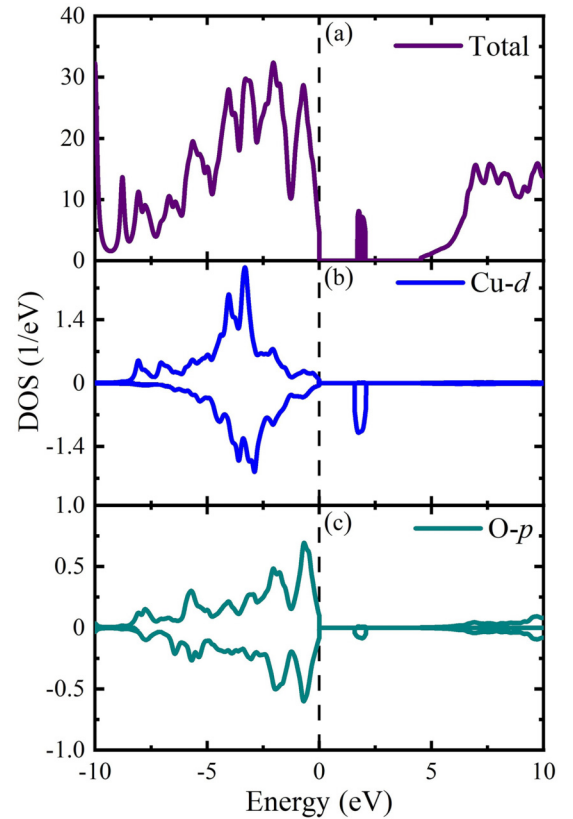


FIG. 13. Density of states (DOS) for the AFM ground state from GGA + U calculations ($U = 6$ eV). (a) Total DOS. (b) Cu- d partial DOS. (c) O- p partial DOS.

effects of Cu- d and O- p orbitals around the Fermi level. Such hybridization effect is visible from the appearance of O- p states [Fig. 13(c)] in the same energy range as Cu- d states. Thus, the correlation effect of the Cu- $3d$ subshell and the formation of local magnetic moments results in the occurrence of an insulating ground state of the material.

IV. CONCLUSIONS

We have grown the single crystalline samples of $\text{BaCu}_2(\text{PO}_4)_2(\text{H}_2\text{O})$ using the hydrothermal technique. Based on the DFT electronic structure calculations, the titled compound has well-separated 1/3-depleted 2D kagome magnetic layers with anisotropic magnetic interactions. The magnetic susceptibility data shows a broad maximum at 25 K. The appearance of a broad maximum in the magnetic susceptibility and heat capacity reveals the low-dimensional nature of the compound. The ^{31}P NMR local probe measurements unambiguously show the presence of magnetic transitions at $T_N = 10.5$ K. The NMR spectrum simulations at 4.7 K suggest the AFM order is incommensurate in nature. The temperature dependence of nuclear spin-lattice relaxation rate ($1/T_1$) exhibits a distinct peak at T_N . While $1/T_1$ falls very steeply below T_N , indicating the disappearance of critical fluctuations, it follows a sub-linear power law behavior above T_N , suggesting the presence of dynamic short-range correlations, which probably stems from the complex 2D spin network

of the compound. A theoretical model on 1/3-depleted 2D kagome lattice is further required to support our experimental findings, especially the incommensurate LRO.

ACKNOWLEDGMENTS

B.K. and S.K.P. acknowledge support from SERB (Grant No. CRG/2023/003063) from DST India. T.C. thanks “KREA Faculty Research Fellowships (2022-2023)” for providing research grants. Work in Tallinn was supported by the “European Regional Development Fund” (Awards TK133 and TK134) and the Estonian Research Council (Projects No. PRG4 and No. PRG1702) for financial support to carry out experiments. K.H.K. and K.-T.K. were financially supported by the Ministry of Science and ICT through the National Research Foundation of Korea (2019R1A2C2090648) and by the Ministry of Education (2021R1A6C101B418).

APPENDIX: MAGIC ANGLE SPINNING – NUCLEAR MAGNETIC RESONANCE (MAS-NMR) SPECTRUM

The high-resolution magic angle spinning (MAS) NMR spectrum is shown to project the difference in the environment of the two phosphorous atoms P1 and P2 (see Fig. 14). It clearly shows that P1 and P2 are different; further analyzing the sideband intensities allows us to determine the principle values of the Knight shift tensor.

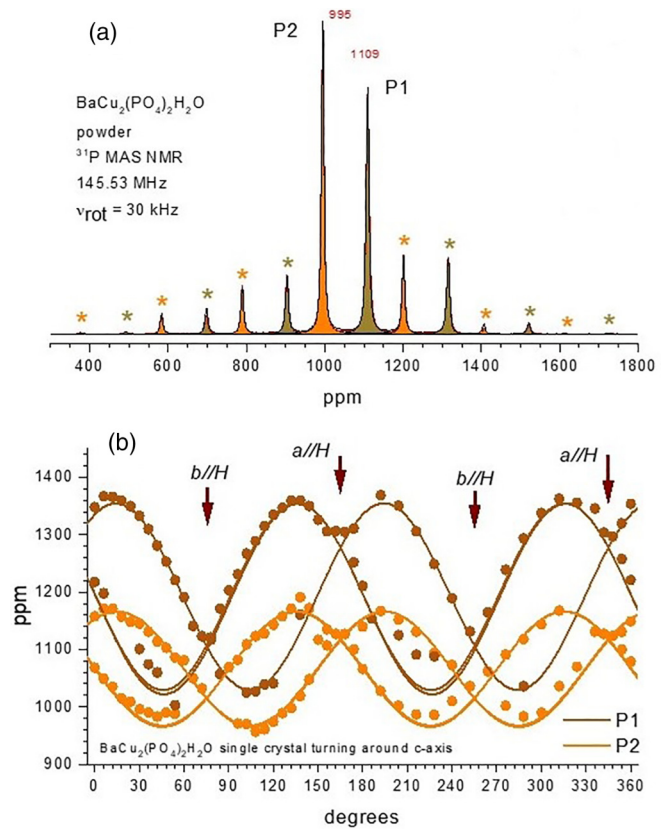


FIG. 14. (a) High-resolution MAS NMR spectrum of powder sample at ambient temperature; the asterisks denote the spinning sidebands at multiple sample spinning frequencies from the main line. (b) The pattern of the resonance frequencies at the rotation of the single crystal about the c axis; the solid lines are calculated positions of the peaks belonging to the P1 sites (brown) and P2 sites (orange).

- [1] A. N. Vasiliev, O. S. Volkova, E. A. Zvereva, and M. Markina, Milestones of low-D quantum magnetism, *npj Quantum Mater.* **3**, 18 (2018).
- [2] M. R. Norman, Colloquium: Herbertsmithite and the search for the quantum spin liquid, *Rev. Mod. Phys.* **88**, 041002 (2016).
- [3] P. Mendels and F. Bert, Quantum kagome antiferromagnet $\text{ZnCu}_3(\text{OH})_6\text{Cl}_2$, *J. Phys. Soc. Jpn.* **79**, 011001 (2010).
- [4] J. Khatua, B. Sana, A. Zorko, M. Gomilšek, K. Sethupathi, M. R. Rao, M. Baenitz, B. Schmidt, and P. Khuntia, Experimental signatures of quantum and topological states in frustrated magnetism, *Phys. Rep.* **1041**, 1 (2023).
- [5] A. Hallett, C. Avarvarei, and J. W. Harter, Combinatorial exploration of quantum spin liquid candidates in the herbertsmithite material family, *Phys. Rev. Mater.* **7**, 064403 (2023).
- [6] T.-H. Han, J. S. Helton, S. Chu, D. G. Nocera, J. A. Rodriguez-Rivera, C. Broholm, and Y. S. Lee, Fractionalized excitations in the spin-liquid state of a kagome-lattice antiferromagnet, *Nature (London)* **492**, 406 (2012).
- [7] B. Fåk, E. Kermarrec, L. Messio, B. Bernu, C. Lhuillier, F. Bert, P. Mendels, B. Koteswararao, F. Bouquet, J. Ollivier, A. D. Hillier, A. Amato, R. H. Colman, and A. S. Wills, Kapellasite: A kagome quantum spin liquid with competing interactions, *Phys. Rev. Lett.* **109**, 037208 (2012).
- [8] P. Khuntia, M. Velazquez, Q. Barthélemy, F. Bert, E. Kermarrec, A. Legros, B. Bernu, L. Messio, A. Zorko, and P. Mendels, Gapless ground state in the archetypal quantum kagome antiferromagnet $\text{ZnCu}_3(\text{OH})_6\text{Cl}_2$, *Nat. Phys.* **16**, 469 (2020).
- [9] M. Fu, T. Imai, T.-H. Han, and Y. S. Lee, Evidence for a gapped spin-liquid ground state in a kagome Heisenberg antiferromagnet, *Science* **350**, 655 (2015).
- [10] F. Bert, S. Nakamae, F. Ladieu, D. L’Hôte, P. Bonville, F. Duc, J.-C. Trombe, and P. Mendels, Low temperature magnetization of the $S = \frac{1}{2}$ kagome antiferromagnet $\text{ZnCu}_3(\text{OH})_6\text{Cl}_2$, *Phys. Rev. B* **76**, 132411 (2007).
- [11] J. S. Helton, K. Matan, M. P. Shores, E. A. Nytko, B. M. Bartlett, Y. Yoshida, Y. Takano, A. Suslov, Y. Qiu, J.-H. Chung, D. G. Nocera, and Y. S. Lee, Spin dynamics of the spin-1/2 kagome lattice antiferromagnet $\text{ZnCu}_3(\text{OH})_6\text{Cl}_2$, *Phys. Rev. Lett.* **98**, 107204 (2007).

- [12] P. Mendels, F. Bert, M. A. de Vries, A. Olariu, A. Harrison, F. Duc, J. C. Trombe, J. S. Lord, A. Amato, and C. Baines, Quantum magnetism in the paratacamite family: Towards an ideal kagomé lattice, *Phys. Rev. Lett.* **98**, 077204 (2007).
- [13] V. A. Zyuzin and G. A. Fiete, Spatially anisotropic kagome antiferromagnet with Dzyaloshinskii-Moriya interaction, *Phys. Rev. B* **85**, 104417 (2012).
- [14] T. Ono, K. Morita, M. Yano, H. Tanaka, K. Fujii, H. Uekusa, Y. Narumi, and K. Kindo, Magnetic susceptibilities in a family of $S = \frac{1}{2}$ kagome antiferromagnets, *Phys. Rev. B* **79**, 174407 (2009).
- [15] S. Owerre, Topological magnetic excitations on the distorted kagomé antiferromagnets: Applications to volborthite, vesignieite, and edwardsite, *Europhys. Lett.* **117**, 37006 (2017).
- [16] B.-J. Yang and Y. B. Kim, Valence bond solid phases on deformed kagome lattices: Application to $\text{Rb}_2\text{Cu}_3\text{SnF}_{12}$, *Phys. Rev. B* **79**, 224417 (2009).
- [17] K. Morita, M. Yano, T. Ono, H. Tanaka, K. Fujii, H. Uekusa, Y. Narumi, and K. Kindo, Singlet ground state and spin gap in $S = 1/2$ kagomé antiferromagnet $\text{Rb}_2\text{Cu}_3\text{SnF}_{12}$, *J. Phys. Soc. Jpn.* **77**, 043707 (2008).
- [18] K. Matan, Y. Nambu, Y. Zhao, T. J. Sato, Y. Fukumoto, T. Ono, H. Tanaka, C. Broholm, A. Podlesnyak, and G. Ehlers, Ghost modes and continuum scattering in the dimerized distorted kagome lattice antiferromagnet $\text{Rb}_2\text{Cu}_3\text{SnF}_{12}$, *Phys. Rev. B* **89**, 024414 (2014).
- [19] M. S. Grbić, S. Krämer, C. Berthier, F. Trouselet, O. Cépas, H. Tanaka, and M. Horvatić, Microscopic properties of the pinwheel kagome compound $\text{Rb}_2\text{Cu}_3\text{SnF}_{12}$, *Phys. Rev. Lett.* **110**, 247203 (2013).
- [20] H. Ishikawa, M. Yoshida, K. Nawa, M. Jeong, S. Krämer, M. Horvatić, C. Berthier, M. Takigawa, M. Akaki, A. Miyake *et al.*, One-third magnetization plateau with a preceding novel phase in volborthite, *Phys. Rev. Lett.* **114**, 227202 (2015).
- [21] H. Yoshida, J.-i. Yamaura, M. Isobe, Y. Okamoto, G. J. Nilsen, and Z. Hiroi, Orbital switching in a frustrated magnet, *Nat. Commun.* **3**, 860 (2012).
- [22] F. Bert, D. Bono, P. Mendels, F. Ladieu, F. Duc, J.-C. Trombe, and P. Millet, Ground state of the kagomé-like $S = 1/2$ antiferromagnet volborthite $\text{Cu}_3\text{V}_2\text{O}_7(\text{OH})_2 \cdot 2\text{H}_2\text{O}$, *Phys. Rev. Lett.* **95**, 087203 (2005).
- [23] Y. Okamoto, H. Yoshida, and Z. Hiroi, Vesignieite $\text{BaCu}_3\text{V}_2\text{O}_8(\text{OH})_2$ as a candidate spin-1/2 kagome antiferromagnet, *J. Phys. Soc. Jpn.* **78**, 033701 (2009).
- [24] A. Zorko, F. Bert, A. Ozarowski, J. van Tol, D. Boldrin, A. S. Wills, and P. Mendels, Dzyaloshinsky-Moriya interaction in vesignieite: A route to freezing in a quantum kagome antiferromagnet, *Phys. Rev. B* **88**, 144419 (2013).
- [25] B. Koteswararao, R. Kumar, J. Chakraborty, B.-G. Jeon, A. Mahajan, I. Dasgupta, K. H. Kim, and F. Chou, $\text{PbCu}_3\text{TeO}_7$: An staircase kagome lattice with significant intra-plane and inter-plane couplings, *J. Phys.: Condens. Matter* **25**, 336003 (2013).
- [26] K. Yoo, B. Koteswararao, J. Kang, A. Shahee, W. Nam, F. F. Balakirev, V. S. Zapf, N. Harrison, A. Guda, N. Ter-Oganessian *et al.*, Magnetic field-induced ferroelectricity in $S = 1/2$ kagome staircase compound $\text{PbCu}_3\text{TeO}_7$, *npj Quantum Mater.* **3**, 45 (2018).
- [27] S. Yoon, C. H. Lee, S. Lee, Y. S. Choi, S.-H. Do, M. Abdel-Jawad, I. Watanabe, B. J. Suh, and K.-Y. Choi, Spin dynamics in the staircase kagome lattice compound $\text{PbCu}_3\text{TeO}_7$, *Phys. Rev. B* **98**, 214401 (2018).
- [28] S. Nishimoto, M. Nakamura, A. O'Brien, and P. Fulde, Metal-insulator transition of fermions on a kagome lattice at 1/3 filling, *Phys. Rev. Lett.* **104**, 196401 (2010).
- [29] K. Ferhat and A. Ralko, Phase diagram of the $\frac{1}{3}$ -filled extended Hubbard model on the kagome lattice, *Phys. Rev. B* **89**, 155141 (2014).
- [30] J. P. Sheckelton, J. R. Neilson, D. G. Soltan, and T. M. McQueen, Possible valence-bond condensation in the frustrated cluster magnet $\text{LiZn}_2\text{Mo}_3\text{O}_8$, *Nat. Mater.* **11**, 493 (2012).
- [31] M. Mourigal, W. T. Fuhrman, J. P. Sheckelton, A. Wartelle, J. A. Rodriguez-Rivera, D. L. Abernathy, T. M. McQueen, and C. L. Broholm, Molecular quantum magnetism in $\text{LiZn}_2\text{Mo}_3\text{O}_8$, *Phys. Rev. Lett.* **112**, 027202 (2014).
- [32] J. P. Sheckelton, F. R. Foronda, L. D. Pan, C. Moir, R. D. McDonald, T. Lancaster, P. J. Baker, N. P. Armitage, T. Imai, S. J. Blundell, and T. M. McQueen, Local magnetism and spin correlations in the geometrically frustrated cluster magnet $\text{LiZn}_2\text{Mo}_3\text{O}_8$, *Phys. Rev. B* **89**, 064407 (2014).
- [33] Y. Haraguchi, C. Michioka, M. Imai, H. Ueda, and K. Yoshimura, Spin-liquid behavior in the spin-frustrated Mo_3 cluster magnet $\text{Li}_2\text{ScMo}_3\text{O}_8$ in contrast to magnetic ordering in isomorphous $\text{Li}_2\text{InMo}_3\text{O}_8$, *Phys. Rev. B* **92**, 014409 (2015).
- [34] K. Iida, H. Yoshida, H. Okabe, N. Katayama, Y. Ishii, A. Koda, Y. Inamura, N. Murai, M. Ishikado, R. Kadono *et al.*, Quantum magnetisms in uniform triangular lattices $\text{Li}_2\text{AMo}_3\text{O}_8$ ($A = \text{In}, \text{Sc}$), *Sci. Rep.* **9**, 1826 (2019).
- [35] S. Nikolaev, I. Solov'yev, and S. Streltsov, Quantum spin liquid and cluster mott insulator phases in the Mo_3O_8 magnets, *npj Quantum Mater.* **6**, 25 (2021).
- [36] G. Chen, H.-Y. Kee, and Y. B. Kim, Cluster Mott insulators and two Curie-Weiss regimes on an anisotropic kagome lattice, *Phys. Rev. B* **93**, 245134 (2016).
- [37] A. Bruker and APEX3, SAINT-Plus, XPREP (2016).
- [38] G. M. Sheldrick, SHELXT-Integrated space-group and crystal-structure determination, *Acta Crystallogr. A* **71**, 3 (2015).
- [39] Sheldrick and G. M., *Shelxl-2018/3 software package*, University of Gottingen, Germany, 2018.
- [40] H. Effenberger, $\text{Sr}_3\text{Cu}_3(\text{PO}_4)_4$, $\text{Pb}_3\text{Cu}_3(\text{PO}_4)_4$, $\text{BaCu}_2(\text{PO}_4)_2 \cdot \text{H}_2\text{O}$, and $\text{Ba}_2\text{Cu}(\text{PO}_4)_2 \cdot \text{H}_2\text{O}$: Crystal structures and topological relationships, *J. Solid State Chem.* **142**, 6 (1999).
- [41] M. Yang, M. Cui, S. Zhang, H. Xiang, W. Guo, and Z. He, Two $S = 1/2$ one-dimensional barium copper phosphates showing antiferromagnetic and ferromagnetic intrachain interactions, *Dalton Trans.* **45**, 3319 (2016).
- [42] J. Rodríguez-Carvajal, Recent advances in magnetic structure determination by neutron powder diffraction, *Physica B* **192**, 55 (1993).
- [43] M. Mekata, T. Hanabata, K. Nakaya, and Y. Ajiro, Quantum spin chain systems with singlet ground state, $\text{ACu}_2(\text{PO}_4)_2$ ($A = \text{Sr}$ and Ba), *J. Magn. Magn. Mater.* **226**, 410 (2001).
- [44] J. B. Goodenough, *Magnetism and the Chemical Bond*, (Interscience-Wiley, New York, 1963).
- [45] R. Nath, A. V. Mahajan, N. Büttgen, C. Kegler, A. Loidl, and J. Bobroff, Study of one-dimensional nature of $S = 1/2$ (Sr, Ba) $_2\text{Cu}(\text{PO}_4)_2$ and BaCuP_2O_7 via ^{31}P NMR, *Phys. Rev. B* **71**, 174436 (2005).
- [46] P. W. Selwood, *Magnetochemistry*, 2nd ed. (Interscience publishers, New York, 1956).

- [47] V. K. Singh, J. Link, K. Kargeti, M. Barik, B. Lenz, N. Saraswat, U. Jena, I. Heinmaa, P. Khuntia, K. Boya, S. K. Panda, R. Stern, Y. Bitla, T. Chakrabarty, and B. Koteswararao, Magnetic properties of $S = \frac{1}{2}$ distorted $J_1 - J_2$ honeycomb lattice compound $\text{NaCuIn}(\text{PO}_4)_2$, *Phys. Rev. B* **107**, 214430 (2023).
- [48] R. Nath, K. M. Ranjith, J. Sichelschmidt, M. Baenitz, Y. Skourski, F. Alet, I. Rousochatzakis, and A. A. Tsirlin, Hindered magnetic order from mixed dimensionalities in CuP_2O_6 , *Phys. Rev. B* **89**, 014407 (2014).
- [49] C. Kittel and P. McEuen, *Introduction to Solid State Physics* (John Wiley & Sons, Hoboken, NJ, 2018).
- [50] P. Bag, N. Ahmed, V. Singh, M. Sahoo, A. A. Tsirlin, and R. Nath, Low-dimensional magnetism of $\text{BaCuTe}_2\text{O}_6$, *Phys. Rev. B* **103**, 134410 (2021).
- [51] S. Yamashita, Y. Nakazawa, M. Oguni, Y. Oshima, H. Nojiri, Y. Shimizu, K. Miyagawa, and K. Kanoda, Thermodynamic properties of a spin-1/2 spin-liquid state in a κ -type organic salt, *Nat. Phys.* **4**, 459 (2008).
- [52] S. Yamashita, T. Yamamoto, Y. Nakazawa, M. Tamura, and R. Kato, Gapless spin liquid of an organic triangular compound evidenced by thermodynamic measurements, *Nat. Commun.* **2**, 275 (2011).
- [53] D. Hirai, K. Nawa, M. Kawamura, T. Misawa, and Z. Hiroi, One-dimensionalization by geometrical frustration in the anisotropic triangular lattice of the 5D quantum antiferromagnet $\text{Ca}_3\text{ReO}_5\text{Cl}_2$, *J. Phys. Soc. Jpn.* **88**, 044708 (2019).
- [54] Y. Haraguchi, A. Matsuo, K. Kindo, and Z. Hiroi, Quantum antiferromagnet bluebellite comprising a maple-leaf lattice made of spin-1/2 Cu^{2+} ions, *Phys. Rev. B* **104**, 174439 (2021).
- [55] S. Zvyagin, A. Ponomaryov, J. Wosnitza, D. Hirai, Z. Hiroi, M. Gen, Y. Kohama, A. Matsuo, Y. Matsuda, and K. Kindo, Dimensional reduction and incommensurate dynamic correlations in the $S = 1/2$ triangular-lattice antiferromagnet $\text{Ca}_3\text{ReO}_5\text{Cl}_2$, *Nat. Commun.* **13**, 6310 (2022).
- [56] K. Nawa, D. Hirai, M. Kofu, K. Nakajima, R. Murasaki, S. Kogane, M. Kimata, H. Nojiri, Z. Hiroi, and T. J. Sato, Bound spinon excitations in the spin-1/2 anisotropic triangular antiferromagnet $\text{Ca}_3\text{ReO}_5\text{Cl}_2$, *Phys. Rev. Res.* **2**, 043121 (2020).
- [57] R. Smith, A. P. Reyes, R. Ashley, T. Caldwell, A. Prokofiev, W. Assmus, and G. Teitel'baum, NMR studies of incommensurate quantum antiferromagnetic state of LiCuVO_4 , *Phys. B: Condens. Matter* **378–380**, 1060 (2006).
- [58] J. M. Law, C. Hoch, R. Glaum, I. Heinmaa, R. Stern, J. Kang, C. Lee, M.-H. Whangbo, and R. K. Kremer, Spin-peierls transition in the $S = \frac{1}{2}$ compound TiPO_4 featuring large intrachain coupling, *Phys. Rev. B* **83**, 180414(R) (2011).
- [59] K. Nawa, M. Takigawa, M. Yoshida, and K. Yoshimura, Anisotropic spin fluctuations in the quasi one-dimensional frustrated magnet LiCuVO_4 , *J. Phys. Soc. Jpn.* **82**, 094709 (2013).
- [60] K. Kimura, P. Babkevich, M. Sera, M. Toyoda, K. Yamauchi, G. Tucker, J. Martius, T. Fennell, P. Manuel, D. Khalyavin *et al.*, Magnetodielectric detection of magnetic quadrupole order in $\text{Ba}(\text{TiO})\text{Cu}_4(\text{PO}_4)_4$ with Cu_4O_{12} square cupolas, *Nat. Commun.* **7**, 13039 (2016).
- [61] R. Rasta, I. Heinmaa, K. Kimura, T. Kimura, and R. Stern, Magnetic structure of the square cupola compound $\text{Ba}(\text{TiO})\text{Cu}_4(\text{PO}_4)_4$, *Phys. Rev. B* **101**, 054417 (2020).
- [62] P. Khuntia, F. Bert, P. Mendels, B. Koteswararao, A. V. Mahajan, M. Baenitz, F. C. Chou, C. Baines, A. Amato, and Y. Furukawa, Spin liquid state in the 3D frustrated antiferromagnet $\text{PbCuTe}_2\text{O}_6$: NMR and muon spin relaxation studies, *Phys. Rev. Lett.* **116**, 107203 (2016).
- [63] A. Smerald and N. Shannon, Angle-resolved nmr: Quantitative theory of ^{75}As T_1 relaxation rate in BaFe_2As_2 , *Phys. Rev. B* **84**, 184437 (2011).
- [64] G. Kresse and J. Hafner, *Ab initio* molecular dynamics for liquid metals, *Phys. Rev. B* **47**, 558 (1993).
- [65] G. Kresse and J. Furthmuller, Efficient iterative schemes for *ab initio* total-energy calculations using a plane-wave basis set, *Phys. Rev. B* **54**, 11169 (1996).
- [66] J. P. Perdew, K. Burke, and M. Ernzerhof, Generalized gradient approximation made simple, *Phys. Rev. Lett.* **77**, 3865 (1996).
- [67] V. I. Anisimov, J. Zaanen, and O. K. Andersen, Band theory and Mott insulators: Hubbard U instead of Stoner I , *Phys. Rev. B* **44**, 943 (1991).
- [68] T. C. Sterling and D. Reznik, Effect of the electronic charge gap on LO bond-stretching phonons in undoped La_2CuO_4 calculated using LDA + U, *Phys. Rev. B* **104**, 134311 (2021).
- [69] P. E. Blochl, O. Jepsen, and O. K. Andersen, Improved tetrahedron method for Brillouin-zone integrations, *Phys. Rev. B* **49**, 16223 (1994).
- [70] N. Marzari and D. Vanderbilt, Maximally localized generalized Wannier functions for composite energy bands, *Phys. Rev. B* **56**, 12847 (1997).
- [71] A. A. Mostofi, J. R. Yates, Y.-S. Lee, I. Souza, D. Vanderbilt, and N. Marzari, wannier90: A tool for obtaining maximally-localised Wannier functions, *Comput. Phys. Commun.* **178**, 685 (2008).
- [72] H. Das, U. V. Waghmare, T. Saha-Dasgupta, and D. D. Sarma, Electronic structure, phonons, and dielectric anomaly in ferromagnetic insulating double perovskite $\text{La}_2\text{NiMnO}_6$, *Phys. Rev. Lett.* **100**, 186402 (2008).
- [73] S. Baidya, P. Sanyal, H. Das, B. Roessli, T. Chatterji, and T. Saha-Dasgupta, Understanding neutron scattering data in YMn_2O_5 : An effective spin Hamiltonian, *Phys. Rev. B* **84**, 054444 (2011).